CHEMISTRY
A EUROPEAN JOURNAL

ChemPubSoc
Europe

DOI: 10.1002/chem.201200864

Synthesis and Characterization of Nanostructured Fe_3O_4 Micron-Spheres and Their Application in Removing Toxic Cr Ions from Polluted Water

Gang Liu,[a] Quan Deng,[a] Huimin Wang,[a] Shenghong Kang,[a] Yong Yang,[a] Dickon H. L. Ng,[b] Weiping Cai,[a] and Guozhong Wang*[a]

Abstract: We present a simple and effective method for the synthesis of nanostructured Fe_3O_4 micron-spheres (NFMSs) by annealing hydrothermally formed $FeCO_3$ spheres in argon. The phase structure, particle size, and magnetic properties of the product have been characterized by X-ray diffraction (XRD), Fourier-transform infrared spectroscopy (FTIR), X-ray photoelectron spectroscopy (XPS), field-emission scanning electron microscopy (FESEM), transmission electron microscopy (TEM), and by means of a superconducting quantum interference device (SQUID). The results have shown that the as-obtained NFMSs have a diameter of about 5 μm and are composed of nanometer-sized porous lamellae. The NFMSs have a large specific surface area (135.9 $m^2 g^{-1}$), reductive Fe^{2+} incorporated into their structure, and intense magnetic properties. These properties suggest that NFMSs have potential application in removing toxic Cr^{6+} ions from polluted water. At 25 °C, each gram of NFMSs product can remove 43.48 mg of Cr^{6+} ions, as compared to just 10.2 mg for nanometer-sized Fe_3O_4 and 1.89 mg for micron-sized Fe_3O_4. The enhanced removal performance can be ascribed to the structural features. Moreover, the Cr^{6+} ion removal capacity of the NFMSs can reach up to 71.2 $mg g^{-1}$ at 50 °C. The influencing parameters in the removal of Cr^{6+} ions, such as contact time, pH, and temperature, have been evaluated. The Cr^{6+}-removal mechanism has been investigated. We have found that the NFMSs product not only serves as an effective adsorbent to remove toxic Cr^{6+} ions from polluted water, but also as an effective reductant in reducing the adsorbed toxic Cr^{6+} ions to much less toxic Cr^{3+} through the Fe^{2+} incorporated into its structure.

Keywords: adsorption · chromium · micron-spheres · nanostructures · water treatment

Introduction

The rapid spread of heavy metal ion pollution in the environment has attracted much public attention due to the toxicity, high mobility, bioaccumulation, and non-biodegradation of these ions.[1] Among the heavy metal ions, the hexavalent chromium (Cr^{6+}) ion has been identified as one of the most toxic species owing to its carcinogenic, mutagenic, and teratogenic features in biological systems.[1b,c] Due to the toxicity of Cr^{6+} ions, Cr^{6+}-containing effluent must be treated before discharge, and the maximum permissible concentration of Cr^{6+} ions in industrial wastewater is 0.25 $mg L^{-1}$.[1d] Many approaches have been developed to treat these toxic Cr^{6+} ions, including adsorption, chemical reduction followed by precipitation, bioremediation, membrane separation processes, reverse osmosis, and ion exchange.[2] However, adsorption only transfers and cannot effectively degrade the Cr^{6+} toxicity to low- or non-toxicity. It must be followed by some secondary treatments. A viable option is to reduce the toxic Cr^{6+} ions with reducing agents (e.g., ferrous sulfate, hydrazine hydrate, or sulfur dioxide), and transform the highly mobile, toxic Cr^{6+} ions into the relatively less mobile and less toxic Cr^{3+}, which is an essential element and its toxicity is about 1000 times lower than that of Cr^{6+} ions.[3] Such a process usually requires subsequent precipitation, which can prove costly and produces a large amount of sludge.[2c,3b] Meanwhile, bioremediation, membrane separation processes, reverse osmosis, and ion exchange are not attractive because of their high operating costs, complex procedures, and strict conditions.[2,4] Thus, there is a pressing need for low-cost, degradable, and recyclable strategies for treating Cr^{6+}-polluted water. It is expected that an agent meeting these requirements will not only remove and degrade toxic Cr^{6+} in one step, but may also be re-used in some simple processes.

Micro-/nanostructured materials, constructed by regularly integrating nano-units to microscale, tend to have superior functions than individual nanometer- and micron-sized materials. They have the advantages of large surface area, high activity, a low tendency for agglomeration, and ease of re-

[a] Dr. G. Liu, Q. Deng, H. Wang, S. Kang, Y. Yang, Prof. W. Cai, Prof. G. Wang
Key Laboratory of Materials Physics
Anhui Key Laboratory of Nanomaterials and Nanotechnology
Institute of Solid State Physics, Chinese Academy of Sciences
Hefei 230031 (P. R. China)
E-mail: gzhwang@issp.ac.cn

[b] Prof. D. H. L. Ng
Department of Physics, The Chinese University of Hong Kong
Shatin, New Territory (Hong Kong)

Supporting information for this article is available on the WWW under http://dx.doi.org/10.1002/chem.201200864.

covery. It has been reported that some common materials, such as silicates, iron oxide, titanium dioxide, and zinc oxide, have been synthesized in different forms of micro-/nanostructures by different methods (e.g., the use of hard/soft templates or surfactants, or through precursor calcinations).[5] These products have been widely used in environmental remediation, and have shown structurally enhanced performances. Compared with many common agents (e.g., active carbon, porous silicon, silicate, titanium dioxide, hematite), magnetite (Fe_3O_4) has some special advantages in treating Cr^{6+} pollution. It is inexpensive, non-toxic, ubiquitous, and environmentally benign. Besides, the outstanding advantage of Fe_3O_4 in environmental remediation is its reductive activity that arises from the presence of bivalent iron in its structure, which can effectively reduce toxic Cr^{6+} to less toxic Cr^{3+}. Moreover, another distinct advantage of Fe_3O_4, compared with non-magnetic materials, in practical environmental remediation is its ease of magnetic recovery, which originates from its intrinsic magnetic property and allows it to be separated from polluted water by means of a magnet.[5c,6] However, nanometer-sized Fe_3O_4 particles can be easily agglomerated, which hinders their capacity for removing Cr^{6+} ions.[6c] Magnetic recyclable Fe_3O_4 in the form of micro-/nanostructures was envisaged as being effective against agglomeration, with high activity as well as enhanced large surface area, making it more favorable to show structurally induced enhanced activity in environmental remediation. The synthesis methods for micro-/nanostructured Fe_3O_4 usually involve the extensive use of surfactants, templates, and costly toxic organic precursors, which are harmful to the environment, making the products unsuitable for wastewater treatment.[7] Therefore, a simple, low-cost, and eco-friendly method will be more favorable for fabricating magnetic micro-/nanostructured Fe_3O_4 to enhance its performance in environmental remediation.

In the present study, NFMSs have been successfully fabricated by annealing hydrothermally formed $FeCO_3$ spheres in argon. During the synthesis, no surfactants, templates, or costly toxic metal or organic reagents were used. The hierarchical character of $FeCO_3$, unlike previously described non-hierarchical morphologies,[8] facilitates the release of gas and the formation of porous structures. Based on the unique hierarchical porous structure with large specific surface area and the reductive Fe^{2+} contained therein, the as-obtained magnetic recyclable NFMSs have been used to clean up Cr^{6+}-induced pollution and showed excellent remediation performance. The parameters affecting Cr^{6+} removal have been studied, such as solution concentration, contact time, pH, and temperature. Based on the adsorption isotherms, the NFMSs showed an obviously structurally enhanced Cr^{6+}-removal capacity ($q_e = 43.48\ mg\,g^{-1}$) at 25 °C compared with their nanometer-sized ($q_e = 10.2\ mg\,g^{-1}$) or micron-sized Fe_3O_4 counterparts ($q_e = 1.89\ mg\,g^{-1}$). The Cr^{6+}-removal capacity of the as-obtained NFMSs reached $q_e = 71.2\ mg\,g^{-1}$ when the temperature was increased to 50 °C.[9] Based on the XPS results, a Cr^{6+}-removal mechanism of adsorption coupled with reduction was proposed. Moreover, the NFMSs could be easily separated from polluted water by means of a magnet, and could be reused after rinsing with ascorbic acid solution.

Results and Discussion

The phase structure and crystal size of the as-obtained NFMSs were determined by XRD, FTIR, and XPS. Figure 1a shows the XRD pattern of the NFMSs obtained after annealing the precursor $FeCO_3$ at 400 °C for 4 h in argon. All of the peaks match well with the standard Fe_3O_4 reflections (JCPDS card no. 76-1849). From Figure S1a (in the Supporting Information), the calculated lattice parameter ($\alpha = 0.839$ nm) is also in good agreement with the standard value ($\alpha = 0.840$ nm) of Fe_3O_4. The average crystal size, estimated from Scherrer's equation based on the full-width at half-maximum of the (311) peak ($2\theta = 35.4°$), was around 12.2 nm.[6d]

FTIR spectroscopy was used to characterize the Fe–O bonds of the as-obtained NFMSs. Fe_3O_4 and γ-Fe_2O_3 have the same cubic inverse spinel structure and can be described as $(Fe^{3+})_A(Fe^{3+}Fe^{2+})_BO_4^{2-}$ and $(Fe^{3+})_A(Fe^{3+}{}_{5/3}\Delta_{1/3})_BO_4^{2-}$, respectively, where Δ denotes a vacancy, and the labels A and B denote the tetrahedral (T_d) and octahedral (O_h) sites, re-

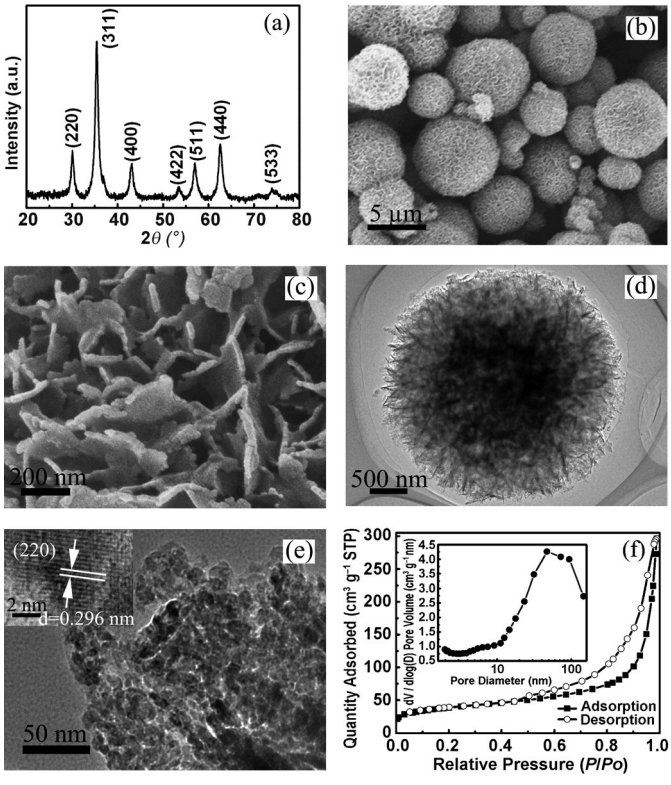

Figure 1. The NFMSs obtained after annealing the precursor $FeCO_3$ at 400 °C for 4 h in argon: a) XRD pattern; b) the general FESEM image; c) high magnification FESEM image; d) TEM image of a single NFMS; e) TEM image of lamellae on the surface of NFMSs and HRTEM image of an NFMS (inset); f) nitrogen adsorption–desorption isotherms and pore size distribution curve (inset) of NFMSs powder.

spectively. Fe_3O_4 is distinct from γ-Fe_2O_3 because of the absence of vacancies in O_h sites.[10] Due to its high sensitivity to vacancy ordering, FTIR analysis can readily distinguish Fe_3O_4 from γ-Fe_2O_3.[10] Figure S1b in the Supporting Information shows typical FTIR spectra of the NFMSs. The strong band at 573 cm^{-1} is characteristic of stoichiometric Fe_3O_4 and can be ascribed to Fe–O deformation in octahedral and tetrahedral sites.[10b,c]

XPS was also used to identify the oxidation state of the Fe 2p (Figure S1c in the Supporting Information). The Fe 2p peaks in γ-Fe_2O_3 are usually accompanied by a characteristic satellite peak on their high-binding-energy side.[11] In contrast, there was no obvious shake-up satellite peak at 719.0 eV in Figure S1c (in the Supporting Information), which was indicative of the Fe_3O_4 phase.[11] In addition, the photoelectron peak, corresponding to Fe $2p_{3/2}$ at 710.7 eV, was in good agreement with the reported value for Fe_3O_4.[11a]

To obtain more information about the structure of the NFMSs, the sample was characterized by electron microscopy. Figure 1b shows a typical FESEM image of the NFMSs, in which large quantities of monodisperse hierarchical spherical structures can be observed, and their diameters are estimated to be about 500–5000 nm. A high-magnification SEM image (Figure 1c) revealed that these NFMSs were composed of numerous ultra-thin nano-lamellae, and that these lamellae were interconnected. Figure 1d shows a typical TEM image of a single NFMS, in which the porous structure can clearly be observed. The selected-area electron diffraction pattern (Figure S2 in the Supporting Information) confirmed that the NFMSs were polycrystalline. From the corresponding HRTEM image (Figure 1e), we found that pores were present in the different nano-building blocks. These results suggested that the NFMSs had highly porous structures. The lattice fringes (inset in Figure 1e) had a spacing of 0.296 nm, corresponding to the (220) lattice plane of Fe_3O_4 (JCPDS card no. 76-1849).

The specific surface area and pore size distribution of the NFMSs were determined by measuring nitrogen adsorption–desorption isotherms (Figure 1f). According to Brunauer–Deming–Deming–Teller classification,[12] the sample exhibited a type H3 hysteresis loop, indicating the presence of pores (2–50 nm). The pore size distribution of the NFMSs (inset in Figure 1f) mainly lay in the meso- and macroporous region. The average pore diameter was about 17.6 nm, and the pore volume was 0.316 $cm^3 g^{-1}$. The Brunauer–Emmett–Teller (BET) specific surface area of the NFMSs was found to be 135.92 $m^2 g^{-1}$, which was higher than that of Fe_3O_4 hollow spherical structures (13.53 $m^2 g^{-1}$) and flower-like Fe_3O_4 nanostructures (34 $m^2 g^{-1}$).[5c,13]

The formation mechanism of the porous NFMSs is discussed in the following. $FeCO_3$ was first produced in a hydrothermal process at 160 °C for 4 h as Equation (1):

$$2CO(NH_2)_2 + 2Fe^{3+} + C_6H_8O_6 + 4H_2O \rightarrow 2FeCO_3 + 4NH_4^+ + C_6H_6O_6 + 2H^+ \quad (1)$$

The $FeCO_3$ was further annealed in argon to produce Fe_3O_4 as Equation (2):

$$3FeCO_3 \rightarrow Fe_3O_4 + 2CO_2\uparrow + CO\uparrow \ \text{(in argon)} \quad (2)$$

Figure S3 (in the Supporting Information) depicts the thermal decomposition process of the $FeCO_3$ spheres in argon. At low temperature, the initial weight loss was mainly due to the release of water adsorbed on the surface of the $FeCO_3$. A sharp weight loss was observed as the temperature reached 200 °C, which continued to 400 °C. The changes were probably due to the thermal decomposition of $FeCO_3$. According to the XRD results, the as-obtained $FeCO_3$ had a rhombohedral structure. Carbonate ions (CO_3^{2-}) have a planar structure and the O–C–O bond angle is 120°. This structure is compatible with the observed symmetry of the ion; the three bonds are equally long and the three oxygen atoms are equivalent. When Fe^{2+} and CO_3^{2-} combine to form $FeCO_3$ crystal nuclei, the iron and oxygen atoms tend to form Fe–O octahedra between the respective planes of CO_3^{2-}. As a result, the generated $FeCO_3$ tends to grow in a lamellar structure during the hydrothermal process (Figure S4 in the Supporting Information). Thus, the as-obtained micro-/nanostructured $FeCO_3$ spheres were composed of narrow nanometer-sized lamellae. The NFMSs were obtained by decomposing the $FeCO_3$ at 400 °C for 4 h in argon as Equation (2).[14] As the reaction proceeded, the release of gaseous CO and CO_2 resulted in the formation of pores in the lamellae (Figure 1e). Fe_3O_4 molecules and small clusters formed crystalline particles, which further grew into nanoparticles under thermal decomposition to form the porous NFMSs (Figure 1d). The formation process is similar to that reported for the growth of corn-like ZnO nanocrystals.[15]

Considering the advantages of large surface area, active Fe^{2+} in the structure, and the magnetic recovery property of NFMSs, they were evaluated for their application in the removal of toxic Cr^{6+} ions from polluted water. The detailed relationships between the Cr^{6+} removal capacity of NFMSs and the concentration of Cr^{6+} ions in solution are illustrated in Figure 2a. We further use Langmuir and Freundlich isotherm models to analyze the experimental data in Figure 2a, as described by Equations (3) and (4), respectively:[16]

$$C_e/q_e = 1/bq_m + C_e/q_m \quad (3)$$

$$\log q_e = \log K_f + 1/n \log C_e \quad (4)$$

in which q_m and b are the Langmuir constants representing the maximum adsorption capacity of adsorbent (mg g^{-1}) and the energy of adsorption, respectively, and K_f and n are the Freundlich constants related to the adsorption capacity and adsorption intensity, respectively. The parameters of the Langmuir and Freundlich models were calculated (as shown in Table S1 in the Supporting Information). From the correlation coefficients (R^2), we noted that the adsorption data fitted the Langmuir isotherm model ($R^2 = 0.997$) quite well

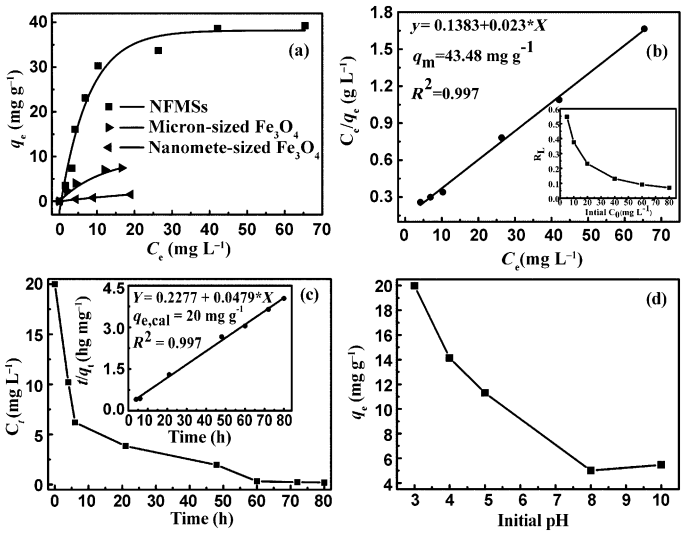

Figure 2. a) Cr^{6+} adsorption curves obtained with different Fe_3O_4 samples. b) Linear Langmuir adsorption isotherm of the NFMSs for Cr^{6+} ions, and plot of the R_L values for Cr^{6+} ion adsorption at different initial concentrations (inset) ($T=25\,°C$, pH 3). c) The time-dependent change of Cr^{6+} ion concentration (20 mg L^{-1}; adsorbent dose: 1 g L^{-1}; pH 3; $T=25\,°C$) in the presence of the as-obtained NFMSs, and the pseudo-second-order kinetic model for Cr^{6+} ion adsorption onto NFMSs (inset). d) Effect of pH on Cr^{6+} removal by NFMSs (the initial concentration of Cr^{6+} was 20 mg L^{-1}; adsorbent dose: 1 g L^{-1}; $T=25\,°C$).

and behaved better than the results using the Freundlich isotherm model ($R^2=0.836$). The curve-fitting result from the Langmuir isotherm model is shown in Figure 2b. It indicated that the adsorption of Cr^{6+} ions onto the NFMSs in this work conformed to a monolayer process. The experimental adsorption capacity ($q_{m,exp}=39.25$ mg g^{-1}) was close to the calculated adsorption capacity ($q_{m,cal}=43.48$ mg g^{-1}) of the Langmuir isotherm model. It was also found that, under the same conditions, the maximum removal capacity of Cr^{6+} ions by the as-obtained NFMSs was far larger than that of nanometer-sized Fe_3O_4 (10.2 mg g^{-1}) or micron-sized Fe_3O_4 (1.89 mg g^{-1}) (Table 1). Moreover, the NFMSs also showed a much higher Cr^{6+} ion removal capacity than other samples, such as the previously reported flower-like Fe_3O_4 nanostructures (4.38 mg g^{-1}), nano Fe_3O_4 (4.72 mg g^{-1}), γ-Fe_2O_3 (3.86 mg g^{-1}), commercial TiO_2 (2.42 mg g^{-1}), activated carbon (3.46 mg g^{-1}), and porous Fe_2O_3/Al_2O_3 nanocomposites (4.01 mg g^{-1}).[5c,6c,17] This enhanced performance in environmental remediation by removing toxic Cr^{6+} ions may be attributed to the novel micro-/nano-hierarchical porous structure (pore volume 0.316 $cm^3 g^{-1}$) and large surface area (135.92 $m^2 g^{-1}$) of the NFMSs. Moreover, the novel hierarchical structure of NFMSs, containing small Fe_3O_4 nanoparticles, helped to foster this effective activity, while their large specific surface area was translated into enhanced capacity for the immobilization and reduction of Cr^{6+} ions. Therefore, the results indicated that the NFMSs used in present study were superior to other reported adsorbents.

Table 1. BET surface areas and Cr^{6+} removal capacities of different Fe_3O_4 samples (adsorbent dose: 1 g L^{-1}; pH 3, $T=25\,°C$; the corresponding morphologies of nanometer- and micron-sized samples can be seen in Figure S5 in the Supporting Information).

Adsorbents	NFMSs	Nanometer-sized Fe_3O_4	Micron-sized Fe_3O_4
BET ($m^2 g^{-1}$)	135.9	85.32	0.99
q_e (mg g^{-1})	43.48	10.2	1.89

The isotherm constant is a parameter that may be used to predict whether an adsorption system is favorable or unfavorable. The essential characteristic of a Langmuir isotherm may be expressed by a term R_L, the dimensionless constant separation factor or equilibrium parameter. R_L reflects the adsorbent capacity and the affinity between the adsorbate and the adsorbent, and is defined according to Equation (5):

$$R_L = 1/(1 + bC_0) \quad (5)$$

in which b and C_0 are the Langmuir constant and the initial concentration of the heavy metal ion, respectively. The inset in Figure 2b shows the calculated R_L value for the adsorption of Cr^{6+} ions onto NFMSs versus the initial concentration of Cr^{6+} ions at 25 °C. The resulting R_L values lie between 0 and 1, clearly indicating that the adsorption of Cr^{6+} ions onto NFMSs was favorable.[16a,18] As the initial Cr^{6+} concentration was increased, the R_L value decreased, indicating that the adsorption was more favorable at higher concentration.[16a,18]

The adsorption kinetics is one of the most important indicators of the rate of uptake of a solute and the adsorption efficiency of the adsorbent. To understand the Cr^{6+} ion adsorption process, the adsorption kinetics was investigated. Figure 2c shows the effect of contact time on the removal of Cr^{6+} ions by NFMSs. Pseudo-first-order and pseudo-second-order kinetic models are employed to interpret the experimental data, as expressed by Equations (6) and (7), respectively:[19]

$$\log(q_e - q_t) = \log q_e - k_1 t/2.303 \quad (6)$$

$$t/q_t = 1/(k_2 q_e^2) + t/q_e \ (k_0 = k_2 q_e^2) \quad (7)$$

in which k_1 (h^{-1}) is the rate constant of the pseudo-first-order adsorption process, k_2 (g mg^{-1} h^{-1}) is the rate constant of the pseudo-second-order model of adsorption, and k_0 (mg g^{-1} h^{-1}) is the initial adsorption rate. For the pseudo-first-order model, the values of k_1 and q_e were calculated from the slope and intercept of plots of $\log(q_e - q_t)$ versus t. For the pseudo-second-order model, the values of k_2 and q_e were obtained from a plot of t/q_t against t. The model equations and their parameter values are listed in Table S2 (in the Supporting Information). The correlation coefficient of the pseudo-second-order kinetic model ($R^2=0.997$) was higher than that of the pseudo-first-order kinetic model ($R^2=0.69$) for the NFMSs. Thus, it would be more accurate to use the pseudo-second-order model to describe the Cr^{6+} ion adsorption process, meaning that the Cr^{6+} removal con-

formed to a chemisorption process. It involved two steps: the electrostatic force attracted the Cr^{6+} ions towards the surfaces of the NFMSs; and the adsorbed toxic Cr^{6+} ions were reduced to less toxic Cr^{3+} by the active Fe^{2+} in the structure of the NFMSs.[18,20]

It was expected that the pH of the medium would have a crucial effect on the Cr^{6+} removal capacity of the NFMSs, because it has a great effect on the surface charge of NFMSs and Cr^{6+} species.[21] Thus, we studied the effect of varying the pH from 3 to 10 on Cr^{6+} removal by the NFMSs. From Figure 2d, it is evident that the NFMSs showed a higher Cr^{6+} removal capacity at lower pH of the aqueous solution. This could be ascribed to the fact that $HCrO_4^-$ ion was the predominant species among the ionic forms of Cr^{6+} at acidic pH, while CrO_4^{2-} ion was the dominant species at alkaline pH.[22] At acidic pH, zeta potential measurement of the isoelectric point (Figure S6 in the Supporting Information) indicated that the surface of the NFMSs was positively charged, which was beneficial for the adsorption of $HCrO_4^-$ ions through electrostatic attraction, leading to a higher removal capacity for Cr^{6+} ions. Otherwise, at alkaline pH, the surface of the NFMSs was negatively charged, leading to electrostatic repulsion between the NFMSs and CrO_4^{2-} ions, resulting in a lower Cr^{6+} ion removal capacity. Moreover, the increased number of OH^- ions would compete with other Cr anions ($HCrO_4^-$ or CrO_4^{2-}) for adsorption sites, further decreasing the Cr^{6+} ion removal capacity of the NFMSs.[16b] Compared with acidic conditions (pH 3), the removal capacity of the NFMSs for Cr^{6+} at pH 8 was reduced to about 30% of the potential reduction capacity, but the Cr^{6+} removal capacity of the NFMSs did not vary significantly when the pH was further increased from 8 to 10 (Figure 2d). This may have been because a buffer layer was formed on the surface of the NFMSs at high pH.[6a,23] However, this did not prevent the NFMSs from showing Cr^{6+} removal capacity superior to that of flower-like Fe_3O_4 nanostructures and other reported adsorbents.[5c,6c,17]

It is known that temperature plays a key role in the adsorption process.[6c,24] The temperature of Cr^{6+}-containing effluents can sometimes exceed 50 °C, hence it is necessary to study the effect of temperature on Cr^{6+} ion removal.[9] In our work, a series of experiments was conducted at 25 °C, 35 °C, and 50 °C. The Cr^{6+} removal capacities of NFMSs at these different temperatures are shown in Table S3 (in the Supporting Information). The Cr^{6+} removal capacity of the NFMSs increased from 43.48 to 71.2 $mg\,g^{-1}$ as the temperature was increased from 25 to 50 °C. This enhanced Cr^{6+} removal capacity of NFMSs may be ascribed to the increase in the vibration frequency of the Cr^{6+} ions at higher temperature. Such an increase would lead to a higher colliding frequency between Cr^{6+} ions and the NFMSs.[24b,c] As a result, more Cr^{6+} ions in the solution were removed by the NFMSs. A similar effect of temperature on Cr^{6+} removal was also observed when Fe_3O_4 nanoparticles were used.[6c]

The morphology of NFMSs after using them to treat Cr^{6+}-polluted water was examined by FESEM and TEM. Images of the sample are shown in Figure 3a and b. We found that the surfaces of the nanometer-sized lamellae of the NFMSs appeared much rougher after treating Cr^{6+}-polluted water, while the surfaces of the as-obtained fresh NFMSs were smooth (Figure 1c). This difference can only be attributed to the deposition of Cr ions on the surface of the NFMSs. The adsorbed Cr^{6+} ions were reduced to Cr^{3+} by Fe^{2+} in the structure of the particles, resulting in the deposition of Cr^{3+} in the form of its oxide or hydroxide on the surface of the NFMSs.[25] EDX analysis revealed the presence of Fe, Cr, O, C, and Cu on the surface of NFMSs after treating Cr^{6+}-polluted water (Figure 3c). Among them, the Fe and O signals originated from the Fe_3O_4 crystals, the C signal was from the carbon film, and the Cu signal was from the copper grid. The spatial distribution of the different constituent elements was clarified by elemental mappings (Figure 3d–f) using the O $K_{\alpha1}$ edge (525 eV), the Fe $K_{\alpha1}$ edge (6399 eV), and the Cr $K_{\alpha1}$ edge (5412 eV), respectively. The spatial distribution of Cr was similar to the distributions of Fe and O, indicating that during the Cr^{6+}-removal process, the NFMSs met the requirements as an effective adsorbing agent to adsorb Cr^{6+} ions due to its large surface area with large pore volume and as a reducing agent to reduce Cr^{6+} through the active Fe^{2+} in its structure. The elemental distribution analysis also demonstrated that Cr compounds had indeed been deposited on the surface of the NFMSs.

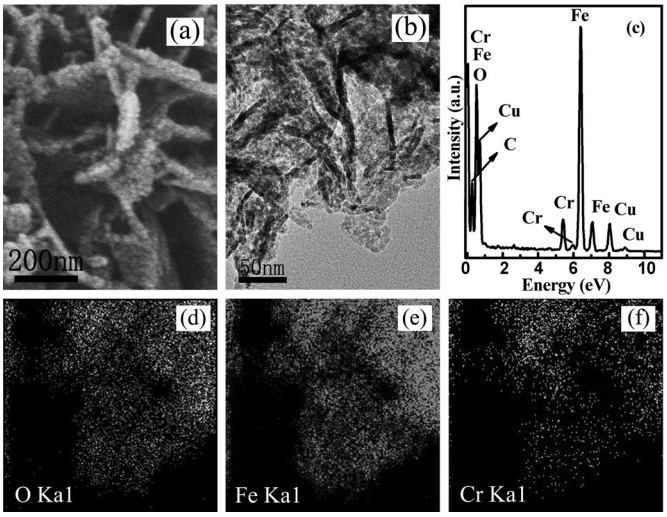

Figure 3. a) FESEM image, b) TEM image, and c) the EDX pattern of the Cr^{6+}-adsorbed surfaces of NFMSs. Elemental maps of O, Fe, and Cr taken from b) are presented in d) at the O $K_{\alpha}1$ edge (525 eV), e) at the Fe $K_{\alpha}1$ edge (6399 eV), and f) at the Cr $K_{\alpha}1$ edge (5412 eV).

XPS was used to further study the oxidation states of Fe and Cr on the surface of Cr^{6+}-adsorbed NFMSs. It was verified that the adsorbed Cr^{6+} ions were reduced by the Fe^{2+} incorporated into the NFMSs (Figure 4). Close inspection of the Fe 2p XPS spectra of the NFMSs before and after adsorption of Cr^{6+} ions revealed that a shake-up satellite peak was observed on the higher-binding-energy side of the main peak after the adsorption, indicated by an arrow in Fig-

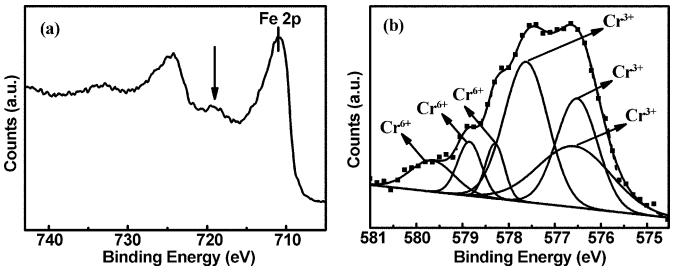

Figure 4. High-resolution XPS spectra of NFMSs after adsorbing Cr^{6+} ions (pH 3, $T=25\,°C$): a) Fe 2p and b) Cr 2p.

ure 4a, whereas it was absent for the smooth surfaces of the NFMSs before adsorption (Figure S1c in the Supporting Information). This satellite peak is a fingerprint of the electronic structure of an Fe^{3+}-containing oxide phase,[11] indicating that an Fe^{3+}-containing oxide phase have been formed on the surface of the NFMSs. This demonstrated that the structural Fe^{2+} in the NFMSs had been partially oxidized to Fe^{3+}, and correspondingly Fe_3O_4 had been partially transformed into Fe_2O_3 during the Cr^{6+} removal process.

The high-resolution XPS spectrum of the Cr 2p region is shown in Figure 4b. The broad peak of Cr $2p_{3/2}$ could be fitted to six peaks at different binding energies: three main peaks at 576.3, 576.5, and 577.6 eV were consistent with the published XPS spectra for the characteristic oxides and hydroxide of Cr^{3+} (i.e., $Cr^{3+}{}_xO_y$ and $Cr(OH)_3$),[26a,b,c] whereas the other three subordinate peaks at 578.3, 578.9, and 579.6 eV corresponded to the characteristic binding energies of adsorbed Cr^{6+} ions.[26d] These results suggested that both Cr^{6+} and Cr^{3+} co-existed on the surface of the NFMSs. From the intensities of the Cr 2p peaks, the majority of the Cr in the overlayer on the surface of NFMSs was in the form of Cr^{3+}, indicating that the removal process of Cr^{6+} by the NFMSs involved adsorption coupled with reduction. The XPS results for Cr 2p under basic conditions were similar to those under acidic conditions (Figure S7 in the Supporting Information), indicating that under the basic conditions the NFMSs could still effectively reduce the toxic Cr^{6+} ions to less toxic Cr^{3+}. These XPS spectra were consistent with a surface redox mechanism: the adsorbed Cr^{6+} ions were reduced to Cr^{3+} on the surface of the NFMSs by electron transfer between the structural Fe^{2+} and Cr^{6+} ions, leading to a coupled oxidation of structural Fe^{2+} to Fe^{3+} and reduction of Cr^{6+} to Cr^{3+}.

Moreover, we further studied the pH changes before and after the removal process. During the Cr^{6+} ion removal process, the pH of the reaction system increased under acidic conditions, which indicated that the Cr^{6+} ion removal process involved the consumption of H^+ according to Equation (8).[27a] Under basic conditions, the pH of the reaction system decreased, which indicated that H^+ was formed in the reaction with Cr^{6+} ions according to Equation (9).[27b] The variation of the final pH in the reaction system with the initial pH can be seen in Table S4 in the Supporting Information. We concluded that the pH changes associated with the Cr^{6+}-removal process could be mainly ascribed to adsorption–reduction co-operation processes. The standard reduction potentials of $E^{\theta}_{\text{chromium(VI)/chromium(III)}}$ and $E^{\theta}_{\text{iron(III)(S)/iron(II)(S)}}$ are 1.51 Vand −0.34 to −0.65 V, respectively,[23a,25a,28] indicating that it was kinetically favorable for the structural Fe^{2+} to reduce adsorbed Cr^{6+} ions.

$$HCrO_4^- + 3Fe^{2+} + 7H^+ \rightarrow Cr^{3+} + 3Fe^{3+} + 4H_2O \quad (8)$$

$$CrO_4^{2-} + 3Fe^{2+} + 8H_2O \rightarrow 4Fe_{0.75}Cr_{0.25}(OH)_3 + 4H^+ \quad (9)$$

On the basis of the above results, we propose a mechanism for Cr^{6+}-removal from polluted water by NFMSs, which involves three steps: 1) mass transfer of Cr^{6+} ions from the bulk solution to the surfaces of NFMSs driven by the initial Cr^{6+} ion concentration difference and electrostatic attraction, 2) adsorption of Cr^{6+} ions at active sites both on the outside and within the surface of the porous structure of the NFMSs, and 3) reduction of the adsorbed Cr^{6+} ions to Cr^{3+} by Fe^{2+} incorporated into the structure of the NFMSs and precipitation of Cr^{3+} in the form of its oxide or hydroxide on the surface of the NFMSs. This phenomenon is consistent with the reported literature.[6c,29] The NFMSs not only effectively remove toxic Cr^{6+} ions from polluted water, but also readily reduce these ions to less toxic Cr^{3+}, alleviating the Cr^{6+}-induced toxicity.

With the rising cost of raw materials, recovery, regeneration, and re-use of adsorbents have become important and an economic necessity. The ferromagnetic behavior of NFMSs makes them easily separable from solution by means of a magnet. The magnetic properties of the NFMSs were measured at room temperature by sweeping the applied magnetic field from −45 to 45 kOe (Figure 5a). The NFMSs showed ferromagnetic behavior with a saturation magnetization (M_s) of about 45 emu g^{-1}. The NFMSs exhibited a hysteretic feature, with the remnant magnetization (M_r) and coercivity (H_c) amounting to 5.68 emu g^{-1} and 66.7 Oe, respectively. Owing to the strong ferromagnetic behavior of NFMSs, the adsorbed contaminant can be easily separated from the solution by means of an external magnet (inset at lower right of Figure 5a), which is much simpler than using centrifugation of non-magnetic adsorbents (e.g., activated carbon, porous silicon, or silicate).[5a,17a,30] At 25 °C, the maximum removal capacity of the NFMSs reached 43.48 mg g^{-1}. When the initial concentration of Cr^{6+} ions was 20 mg L^{-1}, the NFMSs could effectively remove Cr^{6+} ions, and the removal capacity in the first cycle was 19.8 mg g^{-1}, leaving a remaining concentration of about 0.2 mg L^{-1}, which was within the maximum permissible level of Cr^{6+} ions in industrial wastewater.[1d] When the initial concentration of Cr^{6+} ions was reduced to 5 mg L^{-1}, the removal capacity of the NFMSs was 4.73 mg g^{-1}, and the remaining concentration was 0.27 mg L^{-1}, only marginally higher than the maximum permissible level. These results indicated that the NFMSs could effectively remove Cr^{6+} ions, with the remaining concentration lying within the max-

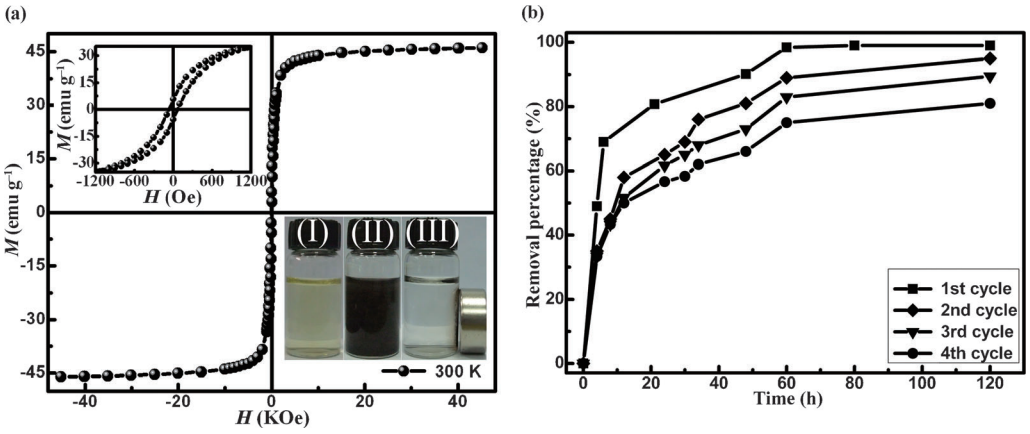

Figure 5. a) Hysteresis loop of NFMSs measured at 300 K, the enlarged magnetization curve between −1200 and 1200 Oe (inset in upper left), and photographs of magnetic separation (inset in lower right): (I) a 20 mg L^{-1} Cr^{6+} solution, (II) a mixture of NFMSs with the 20 mg L^{-1} Cr^{6+} solution; (III) magnetic separation of the NFMSs from the solution after equilibration. b) Cr removal performance of regenerated NFMSs over four cycles (pH 3, $T = 25\,°C$, initial Cr^{6+} concentration: 20 mg L^{-1}, adsorbent dose: 1 g L^{-1}).

imum permissible level between initial concentrations of Cr^{6+} ions of 5–20 mg L^{-1}. Regeneration of the adsorbent is significant for practical treatment of polluted water. After recovery by magnetic separation, the NFMSs bearing adsorbed Cr compounds could be treated by dipping them in aqueous NaOH solution at pH 11 for 1 h, and then in 0.1 mol L^{-1} ascorbic acid solution (8 mL) for 1 h, whereupon they could be re-used. Figure 5b shows the results of Cr^{6+}-removal using the regenerated NFMSs. It was found that the removal efficiency for Cr^{6+} remained at up to 80% after four cycles, which indicated the feasibility of regenerating the NFMSs.

Conclusion

Nanostructured Fe_3O_4 micron-spheres have been prepared by annealing hydrothermally formed $FeCO_3$ spheres assembled from nanometer-sized lamellae, without any requirement for surfactants, templates, or costly toxic organic precursors. The as-obtained NFMSs have spherical architectures with diameters of around 5 μm, and a porous framework composed of many nanometer-sized porous lamellae. The NFMSs are very attractive for the removal of toxic Cr^{6+} ions from polluted water due to their large specific surface area (135.9 $m^2 g^{-1}$), the Fe^{2+} incorporated into their structure, and their magnetic property that allow easy recovery. The Cr^{6+}-removal capacity of NFMSs reached 71.2 mg g^{-1} at 50 °C. Most notably, by virtue of their structure, the NFMSs exhibited enhanced removal performance compared to nanometer- or micron-sized Fe_3O_4. XPS results have clearly shown that the process whereby Cr^{6+} ions are removed by NFMSs involves adsorption coupled with reduction. Thus, the NFMSs not only effectively removed the highly mobile, toxic Cr^{6+} ions from polluted water, but also reduced these ions to less mobile and less toxic Cr^{3+} through the Fe^{2+} incorporated into their structure. Regeneration studies have shown the feasibility of reusing these NFMSs. The results have shown that NFMSs represent a good candidate for efficient Cr^{6+} removal from polluted water.

Experimental Section

Synthesis of NFMSs: In a typical preparation procedure, hexahydrated ferric chloride ($FeCl_3{\cdot}6H_2O$; 4 mmol), ascorbic acid ($C_6H_8O_6$; 4 mmol), and urea ($CO(NH_2)_2$; 10 mmol) were dissolved in deionized water (40 mL) under stirring. The solution was transferred to a Teflon autoclave (70 mL), which was kept at 160 °C for 4 h in an electric oven. After cooling to room temperature, the precipitate was collected by centrifugation and washed with deionized water and ethanol. The precipitate was dried in a vacuum oven at 60 °C for 12 h. For the synthesis of NFMSs, the as-obtained precursor was annealed at 400 °C for 4 h in argon.

Evaluation of water treatment: In the experiment, $K_2Cr_2O_7$ was used as the source of Cr^{6+} ions. Different concentrations of Cr^{6+} ions were prepared and the pH value was adjusted to 3 by using HCl or NaOH. The pH was determined by means of a pH meter (Mettler Toledo SG2-ELK). For each sample solution, 1 g L^{-1} of adsorbent was used. With an agitation speed of 200 rpm at the given temperature, the solid and liquid were separated, and an inductively coupled plasma-optical emission spectrophotometer (ICAP 6000 Thermal Electron) was used to measure the total Cr concentration in the remaining solution. The amount of metal ions adsorbed at adsorption time t (q_t, mg g^{-1}), the amount of metal ions adsorbed at equilibrium (q_e, mg g^{-1}), and the removal percentage (R%) of Cr^{6+} are calculated according to the following equations (10)–(12):[31]

$$q_t = (C_0 - C_t) V\, ms^{-1} \quad (10)$$

$$q_e = (C_0 - C_e) V\, ms^{-1} \quad (11)$$

$$R\,\% = (C_0 - C_t)/C_0 \times 100\,\% \quad (12)$$

in which C_t (mg L^{-1}) is the concentration of Cr^{6+} ions at time t, V is the volume of the solution (L), q_t and q_e (mg g^{-1}) are the amounts of adsorbed Cr^{6+} ions at time t and at equilibrium time, respectively, ms is the mass of adsorbent (g), and C_0 and C_e (mg L^{-1}) are the initial and final concentrations of Cr^{6+} ions, respectively.

Regeneration of NFMSs: The residual NFMSs were collected and soaked in aqueous NaOH solution at pH 11 for 1 h. After rinsing several times with deionized water, the adsorbent was transferred to a 0.1 mol L^{-1} as-

corbic acid solution (8 mL) for 1 h to regenerate the NFMSs. The obtained black product was washed thoroughly with a mixture of deionized water with ethanol and dried in an oven under vacuum at 80 °C for 1 h. The method for testing the capacity of the regenerated NFMSs was the same as in the adsorption experiments above.

Characterization: The samples were analyzed by X-ray diffraction (XRD) over the 2θ range from 20° to 80° using $Cu_{K\alpha}$ radiation (Philips X'pert diffractometer). The surface area of the samples was determined by nitrogen adsorption at 77 K (Micrometrics ASAP 2020M). The morphologies of the samples were studied by field-emission scanning electron microscopy (FESEM, Sirion 200 FEI) and transmission electron microscopy (TEM, JEOL-2010, 200 kV) with an energy-dispersive X-ray spectrometer (EDS, Oxford, Link ISIS). The samples for microscopy studies were prepared by deposition of dispersions of the powder in ethanol directly on the FESEM stubs or holey carbon grid for TEM examination. The isoelectric points of the samples were determined by using a zeta-potential analyzer (Zetasizer 3000HSa). Magnetic measurements of the samples were performed with a superconducting quantum interference device (SQUID) magnetometer (Quantum Design, MPMS XL). Fourier-transform infrared spectroscopy (FTIR) was performed on a JASCO FTIR 410 spectrophotometer. X-ray photoelectron spectroscopy (XPS) of the samples was performed on a Thermo ESCALAB 250 photoelectron spectrometer with $Al_{K\alpha}$ X-rays as the excitation source. Thermal gravimetric (TG) measurements of the samples were carried out on a thermal instrument (Shimadzu Corporation, Japan).

Acknowledgements

This work was supported by the Natural Science Foundation of China (Grant No. 21177132), the Scientific Research Foundation for the Returned Overseas Chinese Scholars, the State Education Ministry, the Special Foundation of President of Hefei Institutes of Physical Science, the Chinese Academy of Sciences, and funded by the CAS Special Grant for Postgraduate Research, Innovation and Practice.

[1] a) L. Zhang, M. Fang, *Nano Today* **2010**, *5*, 128–142; b) M. Cieślak-Golonka, *Polyhedron* **1996**, *15*, 3667–3689; c) S. Basha, Z. V. P. Murthy, B. Jha, *Chem. Eng. J.* **2008**, *137*, 480–488; d) N. Goyal, S. C. Jian, U. C. Banerjee, *Adv. Environ. Res.* **2003**, *7*, 311–319.

[2] a) A. El-Sikaily, A. El Nemr, A. Khaled, O. Abdelwehab, *J. Hazard. Mater.* **2007**, *148*, 216–228; b) T. Karthikeyan, S. Rajgopal, L. R. Miranda, *J. Hazard. Mater.* **2005**, *124*, 192–199; c) S. E. Fendorf, G. Li, *Environ. Sci. Technol.* **1996**, *30*, 1614–1617; d) Y. Cheng, F. Yan, F. Huang, W. Chu, D. Pan, Z. Chen, J. Zheng, M. Yu, Z. Lin, Z. Wu, *Environ. Sci. Technol.* **2010**, *44*, 6357–6363; e) B. Galán, M. Calzada, I. Ortiz, *Chem. Eng. J.* **2006**, *124*, 71–79; f) S. H. Lin, C. D. Kiang, *Chem. Eng. J.* **2003**, *92*, 193–199.

[3] a) M. Gheju, I. Balcu, *J. Hazard. Mater.* **2011**, *196*, 131–138; b) S. E. Fendorf, R. Zasoski, *Environ. Sci. Technol.* **1992**, *26*, 79–85; c) S. Sajjad, S. A. K. Leghari, F. Chen, J. L. Zhang, *Chem. Eur. J.* **2010**, *16*, 13795–13804.

[4] J. Hu, I. M. C. Lo, G. Chen, *Langmuir* **2005**, *21*, 11173–11179.

[5] a) Y. Q. Wang, G. Z. Wang, H. Q. Wang, C. H. Liang, W. P. Cai, L. D. Zhang, *Chem. Eur. J.* **2010**, *16*, 3497–3503; b) Y. Q. Wang, G. Z. Wang, H. Q. Wang, W. P. Cai, L. D. Zhang, *Chem. Commun.* **2008**, 6555–6557; c) L. S. Zhong, J. S. Hu, H. P. Liang, A. M. Cao, W. G. Song, L. J. Wan, *Adv. Mater.* **2006**, *18*, 2426–2431; d) X. W. Duan, G. Z. Wang, H. Q. Wang, Y. Q. Wang, C. Shen, W. P. Cai, *CrystEngComm* **2010**, *12*, 2821–2825; e) Y. M. Cui, L. Liu, B. Li, X. F. Zhou, N. P. Xu, *J. Phys. Chem. C* **2010**, *114*, 2434–2439; f) S. C. Xu, Y. X. Zhang, S. S. Pan, H. L. Ding, G. H. Li, *J. Hazard. Mater.* **2011**, *196*, 29–35.

[6] a) H. A. Wiatrowski, S. Das, R. Kukkadapu, E. S. Ilton, T. Barkay, N. Yee, *Environ. Sci. Technol.* **2009**, *43*, 5307–5313; b) S. Si, C. Li, X. Wang, D. Yu, Q. Peng, Y. Li, *Cryst. Growth Des.* **2005**, *5*, 391–393; c) K. M. M. S. Begum, N. Anantharaman, *Adsorpt. Sci. Technol.* **2009**, *27*, 701–722; d) M. M. Ye, Q. Zhang, Y. X. Hu, J. P. Ge, Z. D. Lu, L. He, Z. L. Chen, Y. D. Yin, *Chem. Eur. J.* **2010**, *16*, 6243–6250.

[7] a) M. Iram, C. Guo, Y. P. Guan, A. Ishfaq, H. Z. Liu, *J. Hazard. Mater.* **2010**, *181*, 1039–1050; b) W. Cheng, K. B. Tang, Y. X. Qi, J. Sheng, Z. P. Liu, *J. Mater. Chem.* **2010**, *20*, 1799–1805; c) Z. B. Huang, F. Q. Tang, *J. Colloid Interface Sci.* **2005**, *281*, 432–436; d) X. Y. Chen, Z. J. Zhang, X. X. Li, C. W. Shi, *Chem. Phys. Lett.* **2006**, *422*, 294–298.

[8] a) L. Z. Wang, F. Q. Tang, K. Ozawa, Z. G. Chen, A. Mukherj, Y. C. Zhu, J. Zou, H. M. Cheng, G. Q. Lu, *Angew. Chem.* **2009**, *121*, 7182–7185; *Angew. Chem. Int. Ed.* **2009**, *48*, 7048–7051; b) S. H. Xuan, L. Y. Hao, W. Q. Jiang, L. Song, Y. Hu, Z. Y. Chen, L. F. Fei, T. W. Li, *Cryst. Growth Des.* **2007**, *7*, 430–434; c) X. J. Liu, H. Wang, C. H. Su, P. W. Zhang, J. B. Bai, *J. Colloid Interface Sci.* **2010**, *351*, 427–432.

[9] Y. T. He, C. C. Chen, S. J. Traina, *Environ. Sci. Technol.* **2004**, *38*, 5535–5539.

[10] a) P. Wu, N. Du, H. Zhang, J. Yu, D. Yang, *J. Phys. Chem. C* **2011**, *115*, 3612–3620; b) R. D. Waldron, *Phys. Rev.* **1955**, *99*, 1727–1735; c) H. Niu, D. Zhang, S. Zhang, X. Zhang, Z. Meng, Y. Cai, *J. Hazard. Mater.* **2011**, *190*, 559–565.

[11] a) M. Basu, A. K. Sinha, S. Sarka, M. Pradhan, S. M. Yusuf, Y. Negishi, T. Pal, *Langmuir* **2010**, *26*, 5836–5842; b) T. Fujii, F. M. F. de Groot, G. A. Sawatzky, F. C. Voogt, T. Hibma, K. Okada, *Phys. Rev. B* **1999**, *59*, 3195–3202.

[12] K. S. W. Sing, D. H. Everett, R. A. W. Haul, L. Moscou, R. A. Pierotti, J. Rouquerol, T. Siemieniewska, *Pure Appl. Chem.* **1985**, *57*, 603–619.

[13] L. P. Zhu, H. M. Xiao, W. D. Zhang, G. Yang, S. Y. Fu, *Cryst. Growth Des.* **2008**, *8*, 957–963.

[14] a) P. L. Fosbøl, K. Thomsen, E. H. Stenby, *Corros. Eng. Sci. Technol.* **2010**, *45*, 115–135; b) A. H. Treiman, *Astrobiology* **2003**, *3*, 369–392.

[15] L. Yang, G. Z. Wang, C. J. Tang, H. Q. Wang, L. D. Zhang, *Chem. Phys. Lett.* **2005**, *409*, 337–341.

[16] a) A. K. Bhattacharya, T. K. Naiya, S. N. Mandal, S. K. Das, *Chem. Eng. J.* **2008**, *137*, 529–541; b) B. H. Hameed, I. A. W. Tan, A. L. Ahmad, *Chem. Eng. J.* **2008**, *144*, 235–244.

[17] a) K. Selvi, S. Pattabhi, K. Kadirvelu, *Bioresour. Technol.* **2001**, *80*, 87–89; b) S. Mor, K. Ravindra, N. R. Bishnoi, *Bioresour. Technol.* **2007**, *98*, 954–957.

[18] K. Y. Shin, J. Y. Hong, J. Jang, *J. Hazard. Mater.* **2011**, *190*, 36–44.

[19] A. R. Kul, H. Koyuncu, *J. Hazard. Mater.* **2010**, *179*, 332–339.

[20] S. S. Liu, Y. Z. Chen, L. D. Zhang, G. M. Hua, W. Xu, N. Li, Y. Zhang, *J. Hazard. Mater.* **2011**, *190*, 723–728.

[21] A. Agrawal, C. Pal, K. K. Sahu, *J. Hazard. Mater.* **2008**, *159*, 458–464.

[22] a) I. J. Buerge, S. J. Hug, *Environ. Sci. Technol.* **1998**, *32*, 2092–2099; b) B. S. Krishna, D. S. R. Murty, B. S. J. Prakash, *J. Colloid Interface Sci.* **2000**, *229*, 230–236.

[23] a) Y. J. Wu, J. H. Zhang, Y. F. Tong, X. H. Xu, *J. Hazard. Mater.* **2009**, *172*, 1640–1645; b) A. G. B. Williams, M. M. Scherer, *Environ. Sci. Technol.* **2001**, *35*, 3488–3494.

[24] a) D. P. Rodda, B. B. Johnson, J. D. Wells, *J. Colloid Interface Sci.* **1996**, *184*, 365–377; b) L. N. Shi, X. Zhang, Z. L. Chen, *Water Res.* **2011**, *45*, 886–892; c) T. Y. Liu, L. Zhao, D. S. Sun, X. Tan, *J. Hazard. Mater.* **2010**, *184*, 724–730.

[25] a) A. F. White, M. L. Peterson, *Geochim. Cosmochim. Acta* **1996**, *60*, 3799–3814; b) M. L. Peterson, A. F. White, G. E. Brown, G. A. Parks, *Environ. Sci. Technol.* **1997**, *31*, 1573–1576; c) L. E. Eary, D. Rai, *Environ. Sci. Technol.* **1988**, *22*, 972–977.

[26] a) L. Dambies, C. Guimon, S. Yiacoumi, E. Guibal, *Colloids Surf. A* **2000**, *177*, 203–214; b) D. Shuttleworth, *J. Phys. Chem.* **1980**, *84*, 1629–1634; c) B. A. Manning, J. R. Kiser, H. Kwon, S. R. Kanel, *Environ. Sci. Technol.* **2007**, *41*, 586–592; d) M. Mullet, F. Demoisson, B. Humbert, L. J. Michot, D. Vantelon, *Geochim. Cosmochim. Acta* **2007**, *71*, 3257–3271.

[27] a) I. J. Buerge, S. J. Hug, *Environ. Sci. Technol.* **1997**, *31*, 1426–1432; b) R. D. Ludwig, C. M. Su, T. R. Lee, R. T. Wilkin, S. D. Acree, R. R. Ross, A. Keeley, *Environ. Sci. Technol.* **2007**, *41*, 5299–5305.
[28] I. V. Goshu, Y. V. Tsarev, V. V. Kostrov, *Russ. J. Appl. Chem.* **2007**, *80*, 2024–2027.
[29] Y. T. He, S. J. Traina, *Environ. Sci. Technol.* **2005**, *39*, 4499–4504.
[30] L. C. Lin, M. Thirumavalavan, Y.-T. Wang, J.-F. Lee, *Colloids Surf. A* **2010**, *369*, 223–231.
[31] L. Sun, L. D. Zhang, C. H. Liang, Z. G. Yuan, Y. Zhang, W. Xu, J. X. Zhang, Y. Z. Chen, *J. Mater. Chem.* **2011**, *21*, 5877–5880.

Received: March 15, 2012
Revised: June 22, 2012
Published online: September 11, 2012

